Nanocrystalline TiO₂/SnO₂ heterostructures for gas sensing

Barbara Lyson-Sypien[*1], Anna Kusior[2], Mieczylaw Rekas[2], Jan Zukrowski[3], Marta Gajewska[3], Katarzyna Michalow-Mauke[4,5], Thomas Graule[4], Marta Radecka[2] and Katarzyna Zakrzewska[1]

Full Research Paper

Address:
[1]AGH University of Science and Technology, Faculty of Computer Science, Electronics and Telecommunications, Al. A. Mickiewicza 30, 30-059 Krakow, Poland, [2]AGH University of Science and Technology, Faculty of Materials Science and Ceramics, Al. A. Mickiewicza 30, 30-059 Krakow, Poland, [3]AGH University of Science and Technology, Academic Center for Materials and Nanotechnology, Al. A. Mickiewicza 30, 30-059 Krakow, Poland, [4]EMPA, Swiss Federal Laboratories for Materials Testing and Research, Laboratory for High Performance Ceramics, Uberlandstrasse 129, 8600 Duebendorf, Switzerland and [5]Paul Scherrer Institut, 5232 Villigen PSI, Switzerland

Email:
Barbara Lyson-Sypien[*] - lyson@agh.edu.pl

* Corresponding author

Abstract

The aim of this research is to study the role of nanocrystalline TiO₂/SnO₂ n–n heterojunctions for hydrogen sensing. Nanopowders of pure SnO₂, 90 mol % SnO₂/10 mol % TiO₂, 10 mol % SnO₂/90 mol % TiO₂ and pure TiO₂ have been obtained using flame spray synthesis (FSS). The samples have been characterized by BET, XRD, SEM, HR-TEM, Mössbauer effect and impedance spectroscopy. Gas-sensing experiments have been performed for H₂ concentrations of 1–3000 ppm at 200–400 °C. The nanomaterials are well-crystallized, anatase TiO₂, rutile TiO₂ and cassiterite SnO₂ polymorphic forms are present depending on the chemical composition of the powders. The crystallite sizes from XRD peak analysis are within the range of 3–27 nm. Tin exhibits only the oxidation state 4+. The H₂ detection threshold for the studied TiO₂/SnO₂ heterostructures is lower than 1 ppm especially in the case of SnO₂-rich samples. The recovery time of SnO₂-based heterostructures, despite their large responses over the whole measuring range, is much longer than that of TiO₂-rich samples at higher H₂ flows. TiO₂/SnO₂ heterostructures can be intentionally modified for the improved H₂ detection within both the small (1–50 ppm) and the large (50–3000 ppm) concentration range. The temperature T_{max} at which the semiconducting behavior begins to prevail upon water desorption/oxygen adsorption depends on the TiO₂/SnO₂ composition. The electrical resistance of sensing materials exhibits a power-law dependence on the H₂ partial pressure. This allows us to draw a conclusion about the first step in the gas sensing mechanism related to the adsorption of oxygen ions at the surface of nanomaterials.

Introduction

The TiO_2–SnO_2 system is extremely important for gas sensing as already proved by many works already published [1-12]. Particularly interesting is the generally accepted possibility of two scenarios: the formation of solid solutions within a certain compositional and temperature range [1,3] or composites of TiO_2 and SnO_2 [4-7]. The fundamental and up till now unresolved question is which form is better for gas sensing.

In fact, we have found in our research that more than two cases are possible. Our previous experience with this system [1,4,6,7,13] indicates that four classes of materials can be obtained:

A. a simple mixture of the constituents denoted as TiO_2–SnO_2

B. perfect solid solutions $Ti_xSn_{1-x}O_2$ where $0 \leq x \leq 1$

C. partially decomposed $Ti_xSn_{1-x}O_2$–$Sn_yTi_{1-y}O_2$ where $0 \leq x \leq 1$ and $0 \leq y \leq 1$

D. decorated nano-heterostructures denoted as $TiO_2@SnO_2$, e.g., TiO_2 nanoflowers overcoated with SnO_2 nanoparticles

Synergetic effects and catalytic reactions can be expected in the case of A) and C) while changes of the morphological and the electronic structure dominate in the case of B) and D). Surface phenomena determine the gas-sensor response in the case of decorated nano-heterostructures, D). As shown in [6], electron transfer over n–n-type heterojunctions can account for sensor sensitization in the cases of A) and D). The formation of n–n-type heterojunctions at the contact between SnO_2 and TiO_2 grains and its effect on the enhancement of the sensor response has been reviewed recently [14].

Figure 1 explains why the formation of n–n heterojunctions between TiO_2 and SnO_2 grains enhances the response of the gas sensor. In fact, the sensitization comes to an effect in the first step of reducing gas detection, namely the preadsorption of oxygen at the grain surface (in our case it is assumed to be in the form of O^- as shown in Figure 1b). The efficiency of the O^- adsorption process is greatly enhanced when a sufficient concentration of electrons is provided. It is usually assumed that SnO_2 grains are more suitable for oxygen adsorption, thus electron transfer from TiO_2 grains is necessary to increase the number of adsorption sites. Electron transfer from TiO_2 to SnO_2 is provided by an appropriate electronic configuration because both conduction (CB) and valence (VB) band edges of TiO_2 are above those of SnO_2 as shown in Figure 1a. The potential difference that is formed when TiO_2 and SnO_2 grains come to contact facilitates electron transport from TiO_2 to SnO_2 thus promoting oxygen preadsorption at the surface of SnO_2 grains.

In the publications about the TiO_2–SnO_2 system [1-12,15-17] for improved gas sensing, one can find different types of materials: thick and thin films, nanostructures such as nanofibers, nanorods, nanobelts, nanopowders as well as core–shell particles. Table 1 presents some of the examples of the latest papers dealing with TiO_2–SnO_2 materials for the detection of different gases.

The performance of a resistive-type gas sensor is inherently related to the form and number of oxygen species adsorbed at the surface of the sensing material in the first step [18]. The equation describing the oxygen chemisorption can be written as [19]:
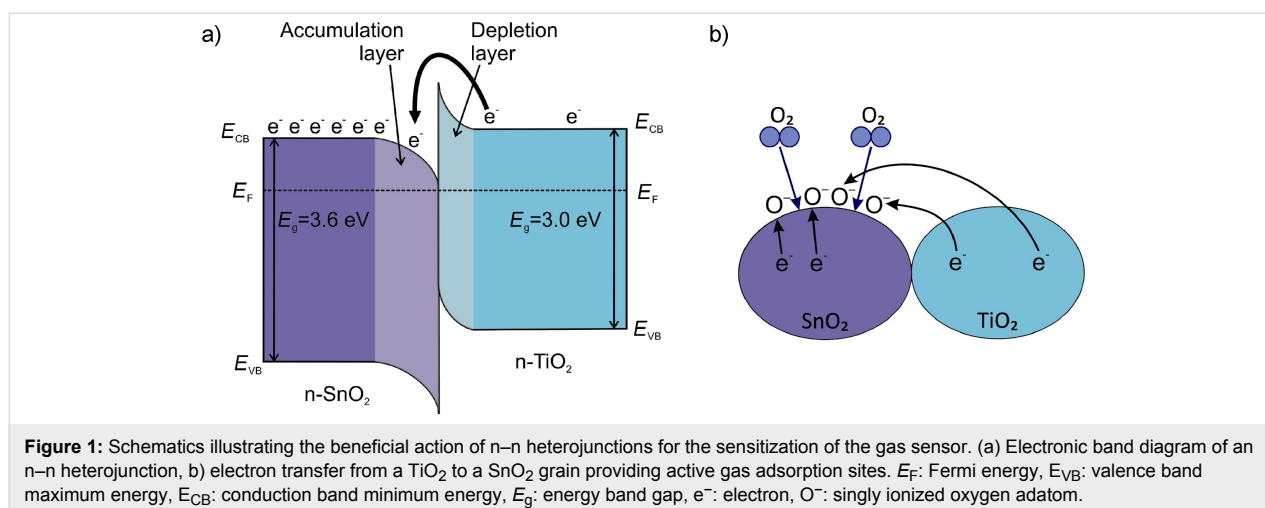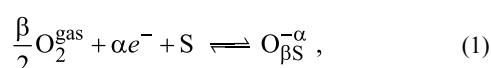
$$\frac{\beta}{2} O_2^{gas} + \alpha e^- + S \rightleftharpoons O_{\beta S}^{-\alpha} , \qquad (1)$$

Figure 1: Schematics illustrating the beneficial action of n–n heterojunctions for the sensitization of the gas sensor. (a) Electronic band diagram of an n–n heterojunction, b) electron transfer from a TiO_2 to a SnO_2 grain providing active gas adsorption sites. E_F: Fermi energy, E_{VB}: valence band maximum energy, E_{CB}: conduction band minimum energy, E_g: energy band gap, e^-: electron, O^-: singly ionized oxygen adatom.

Table 1: TiO_2–SnO_2 systems for gas sensing. The best response is defined either as: R_0/R (for *n*-type material + reducing gas and *p*-type material + oxidizing gas) or R/R_0 (for *n*-type material + oxidizing gas and *p*-type material + reducing gas), where R_0 denotes the electrical resistance in the reference atmosphere and R is the electrical resistance under exposure to the detected gas.

| Form	Method of preparation	Composition/characteristic features	Experimental conditions	Best response	Ref. year
nanopowders	co-precipitation of SnO_2 and TiO_2, mechanical mixing	wt % of SnO_2: 100, 90, 70, 0	H_2 (1–500 ppm) 300–500 °C	R_0/R = 12; 70 wt % SnO_2 + 30 wt % TiO_2; 20 ppm H_2; 400 °C	[2] 2012
	commercial Sigma Aldrich SnO_2 and TiO_2, mechanical mixing	mol % of SnO_2: 100, 95, 90, 80, 50, 20, 10, 2, 0	H_2 (50–3000 ppm) 250–400 °C	R_0/R ≈ 90; 50 mol % SnO_2 + 50 mol % TiO_2; 500 ppm H_2; 325 °C	[4,6] 2013
			NH_3 (100–5000 ppm) 400 °C	R/R_0 = 1.49; 50 mol % SnO_2 + 50 mol % TiO_2; 1200 ppm NH_3; 400 °C	[7] 2012
	sol–gel SnO_2 and TiO_2, mechanical mixing	Ti/Sn: 0, 0.1, 0.3, 0.5, 0.8	VOCs (50–400 ppm) 200–450 °C	R_0/R = 65 Ti/Sn: 0.1; 200 ppm VOCs; ca. 350 °C	[5] 2010
	symplectic gel co-precipitation (SGC)	$Ti_xSn_{1-x}O_2$ (*x*: 0.3, 0.5, 0.7, 0.9)	CO, CH_4, NO_2 (50 ppm) 450–650 °C	R_0/R = 7; $Ti_{0.3}Sn_{0.7}O_2$; 50 ppm CO; 500 °C	[3] 2009
nanofibers	commercial SnO_2 and TiO_2	mol % TiO_2: 100, 90	H_2 (5000–20000 ppm) 300–600 °C	R_0/R ≈ 1.25; TiO_2; 5000 ppm H_2; 500 °C	[8] 2005
polycrystalline ceramics, thin films	solid-state reactions, rf reactive sputtering	$Sn_{1-x}Ti_xO_2$ where *x*: 0, 0.05, 0.1, 0.9, 0.95, 1	H_2 (330–20000 ppm) 400–650 °C	R/R_0 = 2.63; TiO_2; 1000 ppm H_2; 550 °C	[1] 1998
thin films	plasma-enhanced atomic layer deposition	SnO_2 thin films grown on TiO_2 single crystals	H_2, NH_3, CO (100–1000 ppm) 300–500 °C	R_0/R ≈ 380; (101)SnO_2 on (101) TiO_2; 1000 ppm H_2; 400 °C	[9] 2010
thick film	sol–gel	Ti/Sn: 1/7	VOCs (200 ppm) 200–400 °C	R_0/R ≈ 55; Ti/Sn: 1/7; 200 ppm VOCs; 280–360 °C	[10] 2010
coral-like nanostructures	hydrothermal method	coral-like SnO_2 nanostructures modified with TiO_2 nanoparticles	VOCs (50–200 ppm) 200 °C	R_0/R ≈ 12; 200 ppm benzene; 200 °C	[11] 2012
nanorods	thermal evaporation and metal-organic chemical vapor deposition	SnO_2 nanorods with TiO_2 capping	NO_2 (50–100 ppm) 100 °C	R/R_0 = 2.85; 50 ppm NO_2; 100 °C	[15] 2012
nanobelts	hydrothermal method	SnO_2 nanoparticles deposited on TiO_2 nanobelts	VOCs (10–500 ppm) 160–410 °C	R_0/R ≈ 50; 500 ppm acetone; 350 °C	[12] 2015
core–shell	sol–gel	nanocomposite Ti/Sn: 1/1, 1/1.5, 1/2	ethanol (500-5000 ppm) 140-420 °C	R_0/R = 70; Ti/Sn: 1/1.5; 5000 ppm ethanol; 220 °C	[16] 2012
	single-needle electrospinning	hollow SnO_2 nanofibers and core–shell TiO_2–SnO_2 nanofibers	VOCs (10–1000 ppm) 200–370 °C	R_0/R = 55; 1000 ppm ethanol; 300 °C	[17] 2016

where O_2^{gas} is an oxygen molecule in the ambient atmosphere, e^- is an electron that can reach the surface, S is an unoccupied chemisorption site, and $O_{\beta S}^{-\alpha}$ represents chemisorbed oxygen species with α = 1 for singly ionized forms, α = 2 for doubly ionized forms, β = 1 for atomic forms and β = 2 for molecular oxygen.

Table 2 presents possible oxygen species that can be chemisorbed at the surface of the gas sensing material.

Table 2: Possible combinations of α and β and the resulting chemisorbed oxygen species.

	α	β	$O_{\beta S}^{-\alpha}$
molecular	1	2	O_2^-
atomic	1	1	O^-
atomic	2	1	O^{2-}

Hydrogen is considered to react in a second step, at the surface of the oxides, with preadsorbed or lattice oxygen, which, in consequence, increases the electronic conduction. The surface reaction between hydrogen and oxygen can be described in general by the following equation:

$$O_{\beta S}^{-\alpha} + \beta H_{2(g)} = \beta H_2O_{(g)} + \alpha e^-. \qquad (2)$$
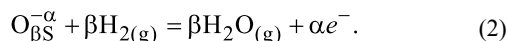
It has been observed that as the result of the two step interaction described above, the electrical resistance, *R*, of the sensor for any reducing gas can be expressed as [1,20]:

$$R \propto p_{gas}^{-n}, \qquad (3)$$

where p_{gas} is the partial pressure of the reducing gas while the power coefficient *n* is specific to the kind of the target gas and particular reaction with oxygen species preadsorbed at the surface of the semiconductor.

In our previous work [1] one can find an analysis of TiO_2–SnO_2 in the form of polycrystalline ceramics and rf-sputtered thin films upon interaction with H_2 but not much is known in the case of nanomaterials. Since that time we have focused on commercial TiO_2 and SnO_2 starting nanomaterials for the sensing of H_2 and NH_3 [4,6,7]. One of the main conclusion from our latest research on commercial materials is that a small addition of TiO_2 to SnO_2 affects gas sensing characteristics to a large extent [4,6]. In this work, for the first time**,** we intend to demonstrate nano-heterostructures of the TiO_2–SnO_2 system prepared by flame spray synthesis with application to gas sensing.

Flame spray synthesis is a well-known and efficient method for the synthesis of crystallized metal oxide nanopowders with particular morphology, e.g., spherical, monodispersed nanoparticles of TiO_2 with good photocatalytic properties [21-23]. However, its application to nano-heterostructures for gas sensing is not known.

The aim of the current work is to study the role of nanocrystalline TiO_2/SnO_2 n–n heterojunctions for hydrogen sensing. Within this work the detailed study on crystallographic structure, morphology, electrical properties, H_2 sensing behavior and the power-law nature of the electrical resistance of TiO_2/SnO_2 heterostructures is presented. The influence of water adsorption and desorption on the electrical properties of TiO_2/SnO_2 is also taken into account. The detection threshold is studied for the first time as a function of the chemical composition of TiO_2/SnO_2 heterostructures.

Experimental

Nanopowders of the TiO_2–SnO_2 system were obtained by flame spray synthesis, FSS, technique using an oxygen–acetylene flame. Not only end compositions, 100 mol % SnO_2 and 100 mol % TiO_2 were prepared. Potential heterostructures of 90 mol % SnO_2/10 mol % TiO_2 and 10 mol % SnO_2/90 mol % TiO_2 were synthesized as well.

Titanium diisopropoxide bis(acetylacetonate) ($TiC_{16}H_{28}O$, 75 wt % in isopropanol, ABCR, CAS: 17927-72-9) and tetramethyltin (CAS: 594-27-4), dissolved in absolute ethanol (C_2H_5OH, 99%, Sigma Aldrich) were used as precursors of titanium and tin, respectively. Details of the FSS setup have been reported elsewhere [24,25].

The required composition and specific surface area (SSA) were obtained by adjusting the ratio of the precursors in the precursor mixture, the total flow rate of which was kept constant at 12.64 $cm^3 \cdot min^{-1}$. The total precursor concentration in the flame was kept constant at 1.5 $mol \cdot kg^{-1}$. The precursor solution was fed by a syringe pump and was atomized with oxygen (583 $cm^3 \cdot s^{-1}$) in a gas-assisted external mixing nozzle. The combustible aerosol was ignited by six oxygen-acetylene flamelets (C_2H_2, 217 $cm^3 \cdot s^{-1}$; O_2, 283 $cm^3 \cdot s^{-1}$) and the produced particles were collected on glass-fiber filters (GF/A 150, Whatman) using vacuum pumps. The nanopowders of TiO_2–SnO_2 did not require any post-synthesis heat treatment since the technique provides well crystallized nanostructures.

The specific surface area (SSA) was determined using Brunauer–Emmett–Teller (BET) nitrogen-adsorption isotherms obtained with a Beckman–Coulter SA3100 apparatus.

The crystallographic structure was analyzed on the basis of XRD patterns recorded in Bragg–Brentano configuration with the help of a Philips X'Pert Pro diffractometer. Based on Rietveld refinement it was possible to determine the weight fractions of cassiterite SnO_2, rutile TiO_2 and anatase TiO_2, the lattice constants and the crystallite sizes, d_{XRD}.

The ^{119}Sn Mössbauer effect measurements were performed in transmission geometry using an MS-4 RENON spectrometer and $CaSnO_3$ as source. The Mössbauer spectra were fitted using a transmission integral in order to take into account the absorber thickness effects. The spectra were refined with quadrupole doublets of Lorentzian lines assuming a non-zero value of the electric field gradient at the tin site. Hyperfine parameters, the isomer shift, *IS*, and quadrupole splitting, *QS*, as well as the full width at half maximum of the Sn peaks, *G*, were found. The values of isomer shift are given relative to the $CaSnO_3$ source kept at room temperature.

Morphology of the synthesized TiO_2–SnO_2 nanomaterials was studied by means of scanning electron microscopy (SEM) performed with a FEI Nova Nano SEM 200 apparatus. High-resolution transmission electron microscopy (HR-TEM) images were obtained using a FEI Tecnai TF 20 X-TWIN microscope. Mapping of chemical elements and diffraction patterns were provided.

The electrical properties were investigated by impedance spectroscopy (IS) in the temperature range from 20 to 550 °C in air. The impedance spectroscopy measurements were performed with a Solatron system (Fra 1260 + dielectric interface 1294). Experimental parameters and data acquisitions were controlled with the FRA software. A frequency range from 1 to 10^6 Hz was covered, with 10 mV amplitude. The impedance spectra were analyzed using the ZView software. An equivalent circuit containing one resistor and a constant phase element (CPE) was used for fitting.

In order to perform gas sensing measurements, the nanosensors were prepared in the form of tablets that were pressed from powders under a pressure of 25 MPa, then annealed at 400 °C and covered with planar silver electrodes. The detailed description of the experimental setup used for the H_2-sensing measurements can be found in [26,27]. The desired hydrogen concentration was obtained by using mass flowmeters mixing synthetic air (reference gas) with H_2 (0.01% H_2, 0.1% H_2, 1% H_2 + Ar depending on the concentration range, i.e., 1–30 ppm, 5–300 ppm and 50–3000 ppm H_2, respectively). The total gas (hydrogen mixture + air) flow rate was kept constant at 120 sccm. The measurements were carried out in dry atmosphere. The synthetic air contained less than 1 ppm of water vapor while that of hydrogen + argon mixture had less than 10 ppm of contaminants. The relative humidity level was verified to be of about 0–1% RH at room temperature.

Dynamic changes in the electrical resistance upon hydrogen exposure have been detected over a low-to-medium concentration range of 1–3000 ppm at a constant temperature between 200 and 400 °C. Measurements within an interval of 1–50 ppm H_2 were performed to determine the hydrogen detection limit. The sensor response S was defined as the ratio between the electrical resistance in the reference atmosphere, R_0, and the electrical resistance upon interaction with hydrogen, R:

$$S = \frac{R_0}{R}. \tag{4}$$

Results and Discussion

Figure 2 shows XRD patterns for SnO_2-rich (Figure 2a) and TiO_2-rich (Figure 2b) heterostructured nanopowders obtained

by FSS compared with the pure end components SnO_2 and TiO_2. Table 3 recapitulates the results of XRD Rietveld refinement performed for TiO_2/SnO_2 nanopowders, and the SSA values determined from BET measurements. The FSS parameters were chosen intentionally in order to obtain approximately the same SSA, and according to the expectation the SSA were found to be within a range of 54–62 $m^2 \cdot g^{-1}$, independent of the chemical composition.

As it can be concluded from Table 3 and Figure 2, pure SnO_2 exhibits the crystallographic structure of cassiterite, whereas in the case of pure TiO_2 two polymorphic forms, anatase and rutile, are present with a predominance of anatase (91.1 wt %). Lattice constants a and c of both TiO_2 and SnO_2 determined experimentally are in good agreement with their theoretical values [28], TiO_2 rutile: $a = 0.45911$ nm, $c = 0.29440$ nm; TiO_2 anatase: $a = 0.37849$ nm, $c = 0.94997$ nm; SnO_2 cassiterite: $a = 0.47360$ nm, $c = 0.31857$ nm.

The main conclusion from Figure 2a is that one can observe a systematic shift of all cassiterite SnO_2 XRD peaks towards higher diffraction angles resulting from a decrease in the lattice constants a and c (Table 3) of the 90 mol % SnO_2/ 10 mol % TiO_2 nanopowder compared with 100% SnO_2. This effect is typical and is usually interpreted as Ti substitution at Sn lattice sites [1]. The absence of non-identified peaks belonging to TiO_2 phases supports the conclusion that under these conditions a solid solution is formed (case B). However, the presence of heterojunctions between the small amount of TiO_2 grains well dispersed within the primary SnO_2 cassiterite phase cannot be excluded.

The influence of 10 mol % SnO_2 in TiO_2 on the XRD pattern (Figure 2b) is much more pronounced. As observed previously for polycrystalline ceramics and thin films [1], even a relatively small amount of SnO_2 in TiO_2 results in a dramatic reconstruction of the crystallographic structure. The content of anatase decreases from 91.1 wt % for pure TiO_2 to 8.5 wt % for 10 mol % SnO_2/90 mol % TiO_2. The crystallite size of anatase remains unchanged (25 nm for 100% TiO_2 and 27 nm for 10 mol % SnO_2/90 mol % TiO_2). The rutile TiO_2 phase begins to predominate (71.1 wt %) with lattice constants slightly higher than those of 100% TiO_2 indicating partially decomposed solid solution (case C). Furthermore, the evidence of precipitation of 18.4 wt % SnO_2 cassiterite with very small crystallites of about 3 nm favors the hypothesis of a heterostructure formation.

In order to study the possible tin oxidation states, Mössbauer spectroscopy was applied. Figure 3 demonstrates transmission spectra of: a) SnO_2; b) 90 mol % SnO_2/10 mol % TiO_2 and c) 90 mol % TiO_2/10 mol % SnO_2 nanopowders.
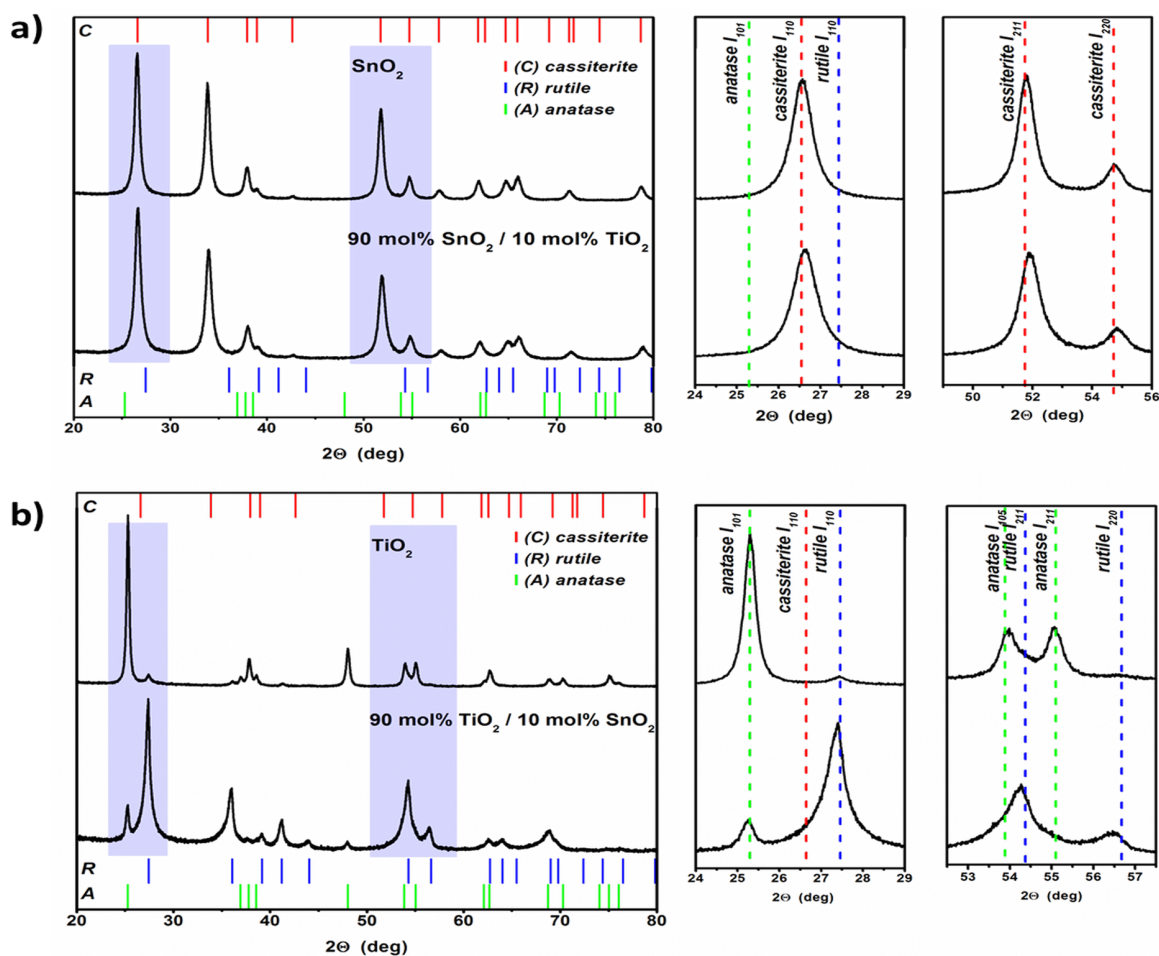
Figure 2: Comparison between XRD patterns of a) SnO$_2$ and 90 mol % SnO$_2$/10 mol % TiO$_2$; b) TiO$_2$ and 90 mol % TiO$_2$/10 mol % SnO$_2$ nanopowders.

Table 3: The results of BET and XRD Rietveld refinement of TiO$_2$–SnO$_2$ nanomaterials; "A" denotes anatase, "R" rutile and "C" cassiterite; SSA: specific surface area.
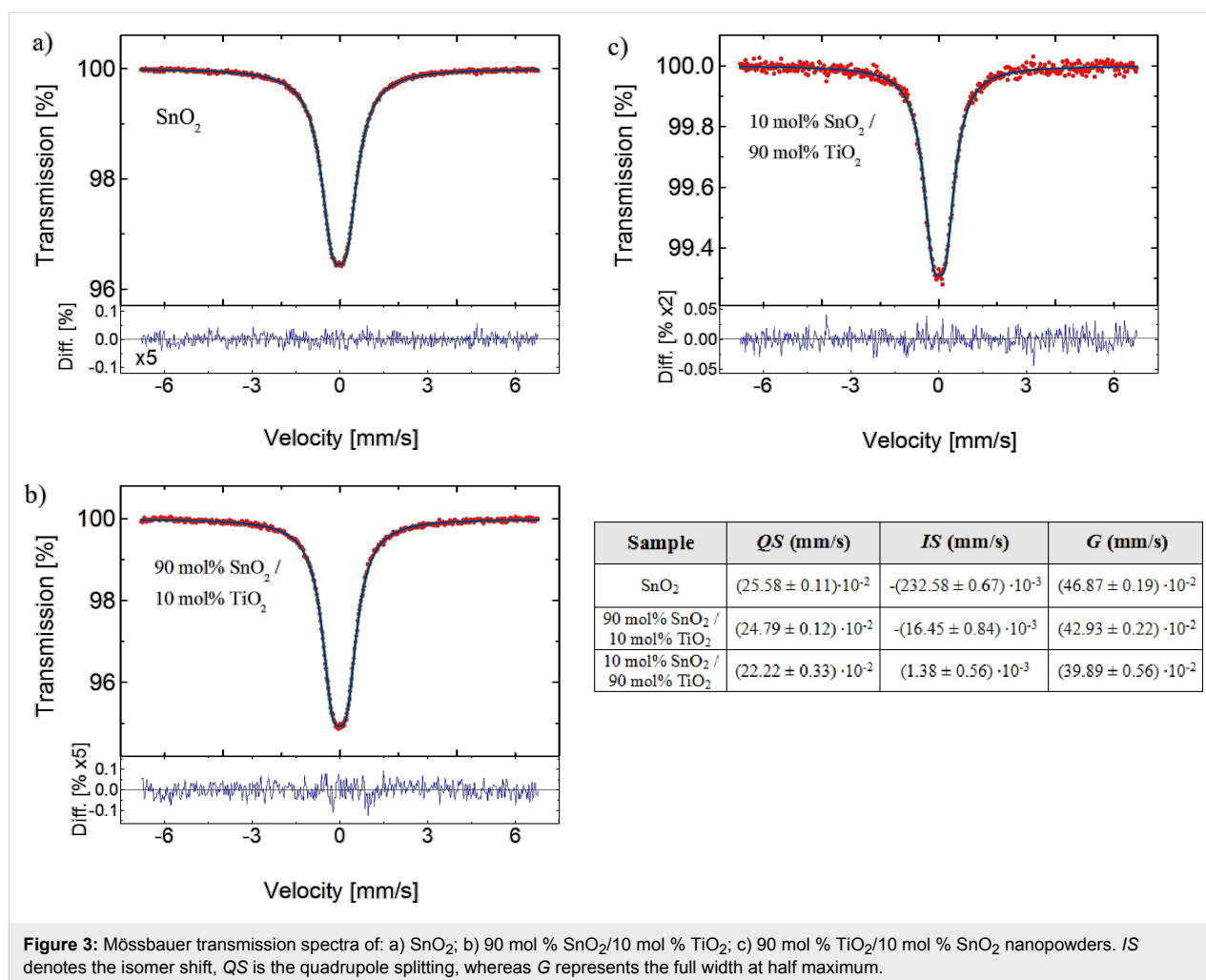
Sample	XRD	C SnO$_2$	A TiO$_2$	R TiO$_2$	SSA (m^2/g)
SnO$_2$	wt %	100			54
	a (nm)	0.47360			
	c (nm)	0.31857			
	crystallite size (nm)	12			
10 mol % TiO$_2$/ 90 mol % SnO$_2$	wt %	100			62
	a (nm)	0.47299			
	c (nm)	0.31780			
	crystallite size (nm)	10			
90 mol % TiO$_2$/ 10 mol % SnO$_2$	wt %	18.4	8.5	73.1	60
	a (nm)	0.45956	0.37840	0.46007	
	c (nm)	0.30447	0.95489	0.29664	
	crystallite size (nm)	3	27	14	
TiO$_2$	wt %		91.1	8.9	57
	a (nm)		0.37849	0.45911	
	c (nm)		0.94997	0.29440	
	crystallite size (nm)		25	15	

The observed peaks are characteristic for Sn^{4+} (SnO_2) for all presented powder samples. No contribution from Sn^{2+} (SnO) has been detected. The measured hyperfine parameters of SnO_2, i.e., the isomer shift, *IS*, and quadrupole splitting, *QS*, at room temperature exhibit similar values for all the studied samples and are in agreement with those reported for SnO_2 [29-31].

Figure 4 shows the dynamic responses of the electrical resistance of 90 mol % SnO_2/10 mol % TiO_2 and 10 mol % SnO_2/ 90 mol % TiO_2 heterostructures upon interaction with hydrogen at a constant temperature of 400 °C. As one can see in Figure 4a and Figure 4c, the electrical resistance decreases upon admission of reducing gas (hydrogen). Thus we can conclude that globally both heterostructures (SnO_2-rich and TiO_2-rich) exhibit n-type conductivity. This is not surprising because usually SnO_2 and TiO_2 are treated as n-type semiconductors [32,33]. Moreover, from the comparison of the gas sensing responses given in Figure 4a and Figure 4c it is easily seen that the heterostructure of 90 mol % SnO_2/10 mol % TiO_2 is very sensitive even to small H_2 concentrations (5–300 ppm H_2,

Figure 4a) while the TiO_2-rich composition, i.e., 10 mol % SnO_2/90 mol % TiO_2 requires higher hydrogen concentrations (50–3000 ppm H_2, Figure 4c).

SEM and HR-TEM images, as well as the results of selected area electron diffraction (SAED) and mapping of elements are given in Figure 4b and Figure 4d for the gas sensing materials given in Figure 4a and Figure 4c, respectively. There are some differences between the microstructure of 90 mol % SnO_2/ 10 mol % TiO_2 and 10 mol % SnO_2/90 mol % TiO_2. In the case of TiO_2-rich heterostructures the grains are larger and spherical (Figure 4d), while for SnO_2-rich compositions grains are smaller, more irregular in shape and elongated (Figure 4b). The spherical nanograins of TiO_2 are probably composed of smaller crystallites while separate SnO_2 grains were not identified by SAED for 10 mol % SnO_2/90 mol % TiO_2. Element mapping suggests that a small amount of Sn (Figure 4d) is finely dispersed within the TiO_2 matrix. In the 90 mol % SnO_2/ 10 mol % TiO_2 heterostructures Ti is well incorporated into SnO_2 building blocks (Figure 4b).
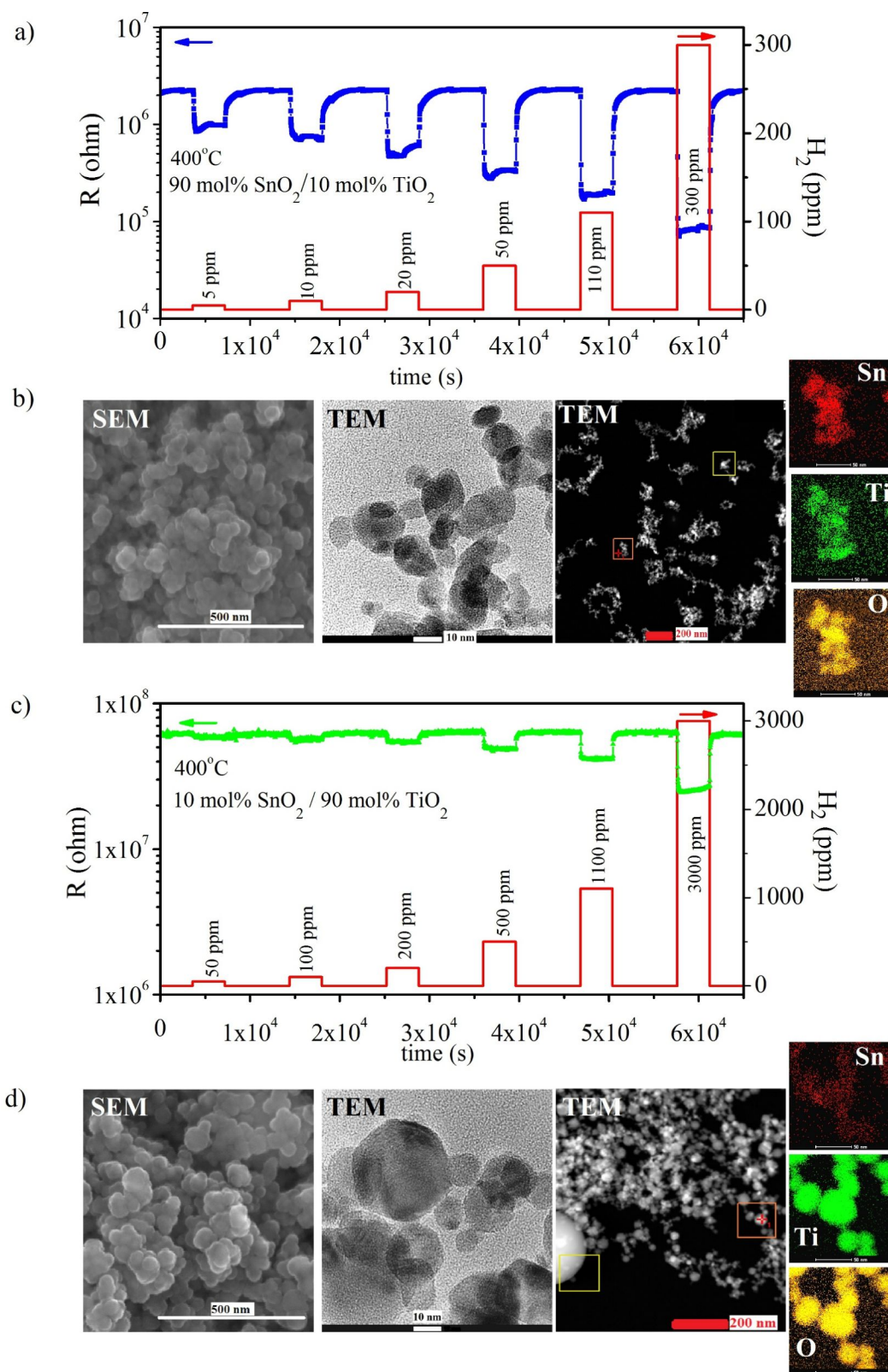

Sample	*QS* (mm/s)	*IS* (mm/s)	*G* (mm/s)
SnO_2	$(25.58 \pm 0.11) \cdot 10^{-2}$	$-(232.58 \pm 0.67) \cdot 10^{-3}$	$(46.87 \pm 0.19) \cdot 10^{-2}$
90 mol% SnO_2 / 10 mol% TiO_2	$(24.79 \pm 0.12) \cdot 10^{-2}$	$-(16.45 \pm 0.84) \cdot 10^{-3}$	$(42.93 \pm 0.22) \cdot 10^{-2}$
10 mol% SnO_2 / 90 mol% TiO_2	$(22.22 \pm 0.33) \cdot 10^{-2}$	$(1.38 \pm 0.56) \cdot 10^{-3}$	$(39.89 \pm 0.56) \cdot 10^{-2}$

Figure 3: Mössbauer transmission spectra of: a) SnO_2; b) 90 mol % SnO_2/10 mol % TiO_2; c) 90 mol % TiO_2/10 mol % SnO_2 nanopowders. *IS* denotes the isomer shift, *QS* is the quadrupole splitting, whereas *G* represents the full width at half maximum.

Figure 4: Dynamic changes in the electrical resistance, *R*, of: a) 90 mol % SnO_2/10 mol % TiO_2 (H_2 concentration: 5–300 ppm) and c) 10 mol % SnO_2/90 mol % TiO_2 (H_2 concentration: 50–3000 ppm) nanomaterials upon interaction with hydrogen at a constant temperature of 400 °C along with the corresponding SEM and TEM images (b, d). Step changes in hydrogen concentrations are given on the right hand scale (a, c).

Driven by the promising sensor signal for the step changes in H_2 concentration (Figure 4), we decided to perform additional measurements in order to determine the hydrogen detection threshold for the studied TiO_2/SnO_2 heterostructures. Figure 5a and Figure 5b present dynamic changes in the electrical resistance of 90 mol % SnO_2/10 mol % TiO_2 and 10 mol % SnO_2/90 mol % TiO_2, respectively, upon interaction with 1 and 2 ppm H_2. The H_2 detection threshold for the studied TiO_2/SnO_2 heterostructures is lower than 1 ppm, especially in the case of SnO_2-rich composition (Figure 5a). As one discusses 10 mol % SnO_2/90 mol % TiO_2 it appears that at 1 ppm H_2 the signal-to-noise ratio becomes much worse. However, the sensor signal is still discernible.

Within the studied temperature range SnO_2-rich nanomaterials exhibit better gas-sensing performance (Figure 5c,d). The larger sensor response, R_0/R (by about 20 times) for SnO_2-rich heterostructures compared to TiO_2-rich ones is typical as titanium dioxide requires higher temperatures for improved sensing characteristics.

In Figure 5c and Figure 5d one can also analyze the influence of the formation of heterostructures on the sensor response, R_0/R. In both cases the sensor response increases compared to the pure oxides. The improvement in gas-sensing by a small addition of TiO_2 to SnO_2 was reported previously [5]. The explanation of this phenomenon is based on the charge transfer be-
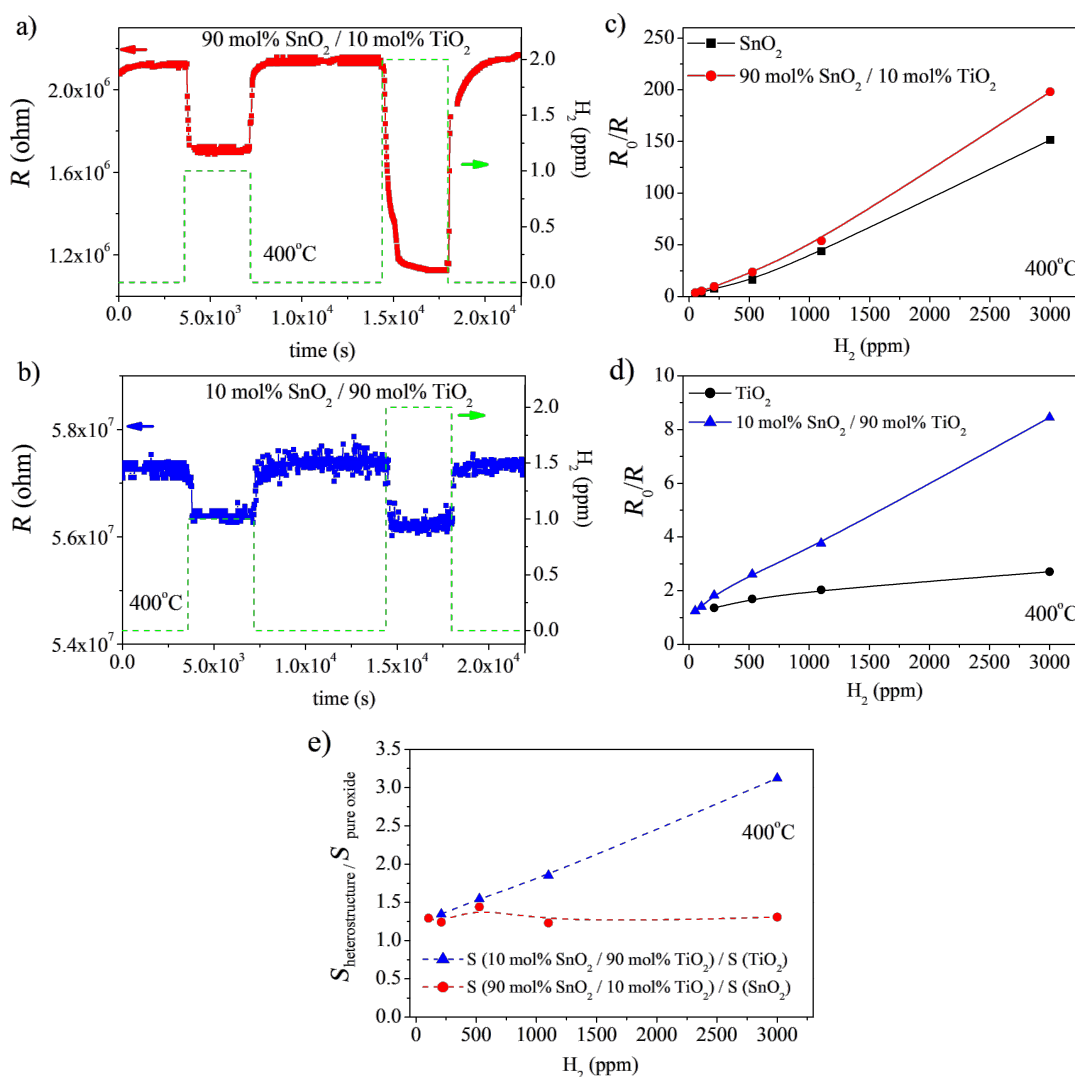

Figure 5: Dynamic changes in the electrical resistance, *R*, of: a) 90 mol % SnO_2/10 mol % TiO_2; b) 10 mol % SnO_2/90 mol % TiO_2 nanomaterials upon interaction with 1 and 2 ppm of H_2 along with the corresponding sensor response (R_0/R) as a function of H_2 concentration (c, d). The influence of the formation of heterostructures on the gas-sensing performance is given in e) as the corresponding ratio of responses $S_{heterostructure}$ normalized to those of pure SnO_2 and TiO_2 ($S_{pure\ oxide}$). The gas-sensor response *S* is defined in Equation 4.

tween TiO_2 and SnO_2 due to the differences in the positions of the conduction and valence band edges of both oxides (Figure 1). A similar effect was reported in our previous work for 2 mol % TiO_2/98 mol % SnO_2 nanocomposites working as H_2 sensors [4].

In this work, for the first time, based on Figure 5e, we can conclude that the addition of SnO_2 to TiO_2 (10 mol % SnO_2/ 90 mol % TiO_2) has a much more pronounced effect than the addition of TiO_2 to SnO_2 (90 mol % SnO_2/10 mol % TiO_2). Moreover, one should also take into account the kinetics of interaction described by response and recovery times.

Despite the fact that SnO_2-rich heterostructures exhibit larger responses to gases over the whole measuring range, it appears that their recovery time, τ, for the sensor to reach 90% of the initial electrical resistance, R_0, is much longer than that of TiO_2-rich heterostructures at higher H_2 concentrations (Figure 6). In the case of 90 mol % SnO_2/10 mol % TiO_2 (1100 ppm H_2), τ is about 2500 s, whereas for 10 mol % SnO_2/90 mol % TiO_2 (1100 ppm H_2), τ is less than 30 s. The longer recovery time of SnO_2-rich sensors can be attributed to a constricted gas desorption that probably results from the differences in the microstructure evidenced by SEM (Figure 4).

A fast desorption process is a prerequisite for the reproducible response and from this point of view TiO_2-rich heterostructures exhibit better performance at higher H_2 concentrations (1000–3000 ppm). From the analysis presented in Figure 5 and Figure 6 one can make the conclusion that TiO_2/SnO_2 nanoheterostructures can be intentionally modified by changing the chemical composition in order to meet requirements for successful detection of both small (SnO_2-rich content) and large H_2 concentrations (TiO_2-rich compositions).

Figure 7 demonstrates the temperature variation of the electrical resistance in the reference gas (air), R_0, its value upon interaction with 100 ppm H_2, R, as well as the sensor response defined as a ratio of R_0/R for the two compositions of 90 mol % SnO_2/10 mol % TiO_2 (Figure 7a,b) as well as 10 mol % SnO_2/90 mol % TiO_2 (Figure 7c,d).

It can be seen that R_0 decreases with increasing operating temperature. As for R, it seems that this effect is more pronounced for the TiO_2-rich sample. In the case of the SnO_2-rich composite the electrical resistance R upon interaction with 100 ppm H_2 seems to be independent of the temperature. For 90 mol % SnO_2/10 mol % TiO_2, the temperature dependence of R_0/R follows R_0 vs temperature, because R is almost constant. On the other hand, in the case of the TiO_2-rich sample both R_0 and R exhibit a similar temperature dependence, which leads to a gas response R_0/R almost independent of the temperature.

In order to study the electrical properties of TiO_2/SnO_2, impedance spectroscopy was applied. Figure 8 presents: a) the impedance spectra obtained at 400 °C as well as the electrical resistance as a function of the temperature for: b) 90 mol % SnO_2/ 10 mol % TiO_2 and c) 10 mol % SnO_2/90 mol % TiO_2.

The impedance spectra (IS) in Nyquist representation (Figure 8a) consist of a well-developed semicircle, followed by a deformed semicircle at lower frequencies. The equivalent circuit fitted to all spectra is a loop composed of one resistor R in parallel with a constant phase element CPE. Resistor R and CPE represent the bulk/surface process and their values have been determined by fitting (Figure 8a). The CPE in the majority of cases resembles a Debye capacitor C. The resulting electrical resistance R as a function of temperature exhibits a maximum, the position of which T_{max} depends on the competing processes
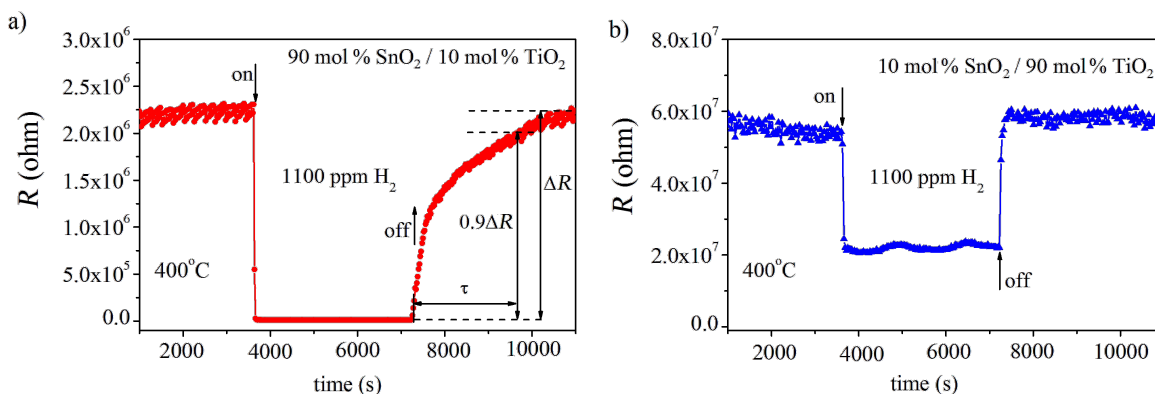

Figure 6: Dynamic changes in the electrical resistance, *R*, of: a) 90 mol % SnO_2/10 mol % TiO_2; b) 10 mol % SnO_2/90 mol % TiO_2 heterostructures upon interaction with 1100 ppm H_2. τ denotes the recovery time.
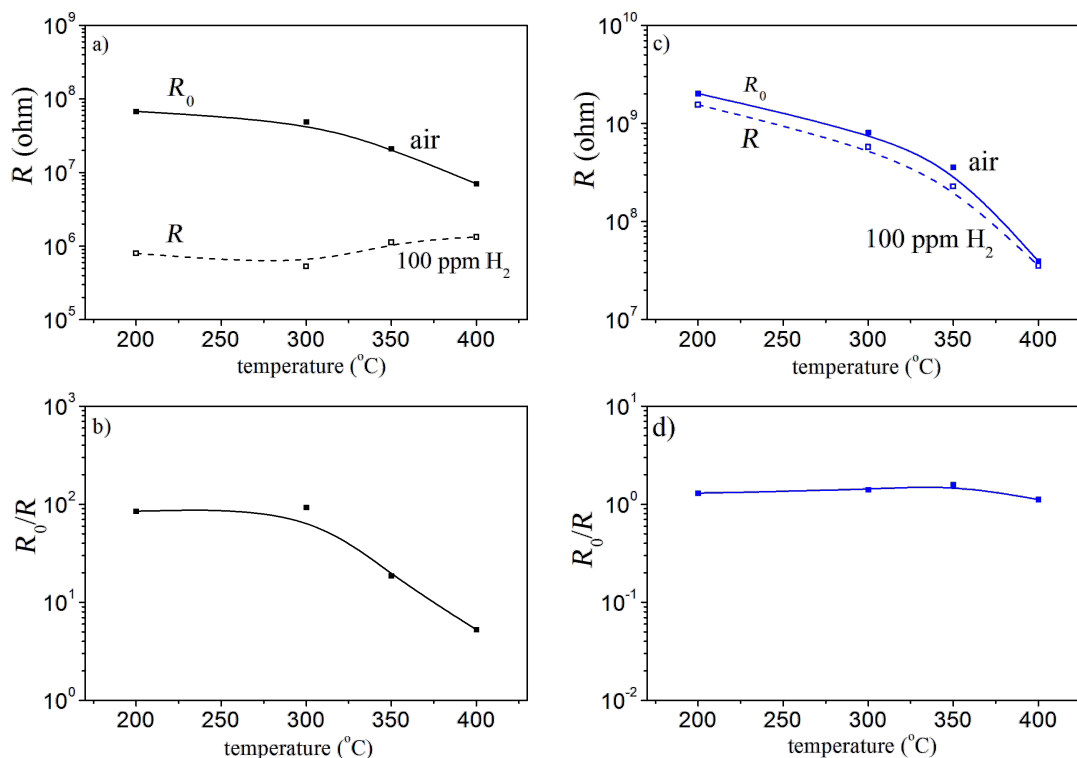
Figure 7: Temperature dependence of the electrical resistance in air, R_0, compared with that upon interaction with 100 ppm H_2, R, together with the sensor response, R_0/R, for the samples of 90 mol % SnO_2/10 mol % TiO_2 (a, b) and 90 mol % TiO_2/10 mol % SnO_2 (c, d).

water desorption, oxygen adsorption and semiconducting behavior at higher temperatures. As can be seen in Figure 8b, for SnO_2-rich heterostructures T_{max} is about 100–125 °C, while for TiO_2-rich heterostructures as shown in Figure 8c, T_{max} is much higher within the range of 200–250 °C.

From the thermodynamics of chemical reactions it is well known that oxygen adsorption (described, e.g., by the coverage degree Γ) is an exothermic process and decreases with temperature [34]. Under the experimental conditions this situation is given when the adsorption processes remain in thermodynamic equilibrium, i.e., at temperatures larger than a characteristic value T_{eq}. In the case of oxygen adsorption at the surface of oxides, T_{eq} is of the order of 400 °C [35]. At temperatures smaller than T_{eq} the coverage degree Γ increases with temperature as described by the laws of chemical kinetics.
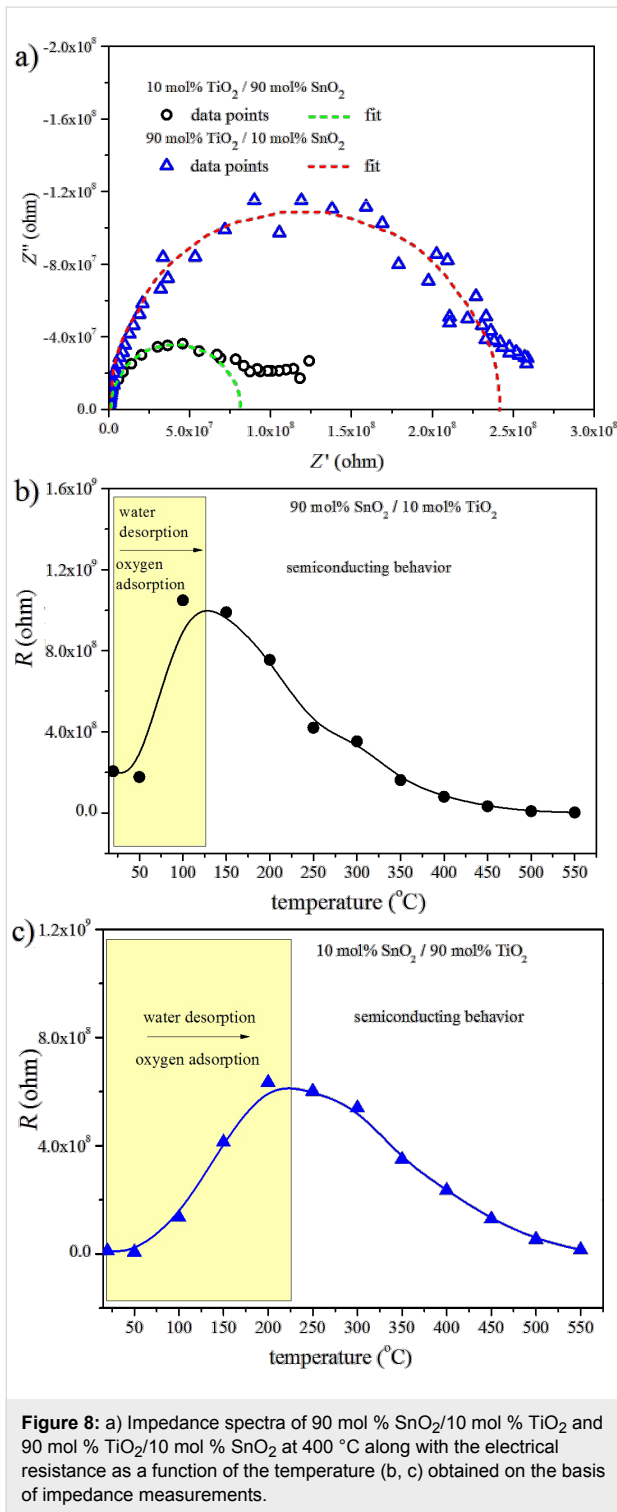
The interpretation of the results given in Figure 8, assuming that the resistance changes are related only to the gas adsorption, is based on the fact that the experimental T_{max} is much smaller than the theoretically predicted T_{eq}. At these relatively low temperatures water desorption is believed to predominate over oxygen adsorption. However, both processes are possible. In the literature one can find three types of mechanisms explaining the

increase in the surface conductivity in the presence of water vapor as in all these cases the electron concentration is increased [36]. Water adsorption becomes important at temperatures below T_{max} and certainly at room temperature.
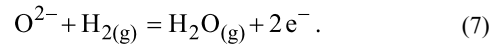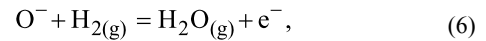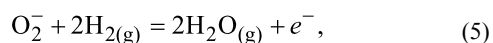
The subsequent increase in the temperature above 100–200 °C (see Figure 8b,c) leads to a decrease in the electrical resistance, which is a typical effect for semiconductors and is related to the creation of additional charge carriers.

The temperature T_{max} at which the semiconducting behavior begins to prevail over water desorption/oxygen adsorption depends on the TiO_2–SnO_2 composition. The higher T_{max} for TiO_2-rich heterostructures can be explained on the basis of the higher ionic defect concentration (mainly oxygen vacancies) at the surface of TiO_2. It is well known that oxygen vacancies act as water adsorption centers. Moreover, in the case of SnO_2 water adsorption takes place because of the formation of weak van der Waals bonds between water dipoles and lattice ions (Sn^{4+} and O^{2-}) [19]. This facilitates water desorption from the surface of SnO_2-rich heterostructures at lower temperatures.

As one discusses the interaction between the gas phase and the semiconducting sensor, the two-step mechanism described in

$$O^- + H_{2(g)} = H_2O_{(g)} + e^-, \qquad (6)$$

$$O^{2-} + H_{2(g)} = H_2O_{(g)} + 2\,e^-. \qquad (7)$$

Applying the law of mass action to Equations 5–7 yields:

$$n_e = \frac{K_1}{\left(p_{H_2O}\right)^2}\left(p_{H_2}\right)^2, \qquad (8)$$

$$n_e = \frac{K_2}{p_{H_2O}}\,p_{H_2}, \qquad (9)$$

$$n_e = \frac{K_3}{\left(p_{H_2O}\right)^{1/2}}\left(p_{H_2}\right)^{1/2}, \qquad (10)$$

where n_e denotes the concentration of electrons, and K_1, K_2, K_3 are the equilibrium constants of the reactions described by Equations 5–7. The concentration of adsorbed oxygen is assumed to remain constant during its interaction with hydrogen. This is justified by $p_{O2} \gg p_{H2}$ and a high rate of oxygen chemisorption under the experimental conditions [1].

As the electron mobility μ_e is practically independent of the gas partial pressure, and the relationship for the electrical resistivity reduces to $\rho = 1/(e{\cdot}\mu_e{\cdot}n_e)$ for n-type semiconductors, the $1/R(p_{H2})$ dependence assumes the same form as $n_e(p_{H2})$ does (Equations 8–10). Thus, $n = 1/2, 1$ or 2 are theoretically predicted for different oxygen species preadsorbed on the surface of the semiconductor.

In the case of formation of oxygen vacancies V_O, the following reaction could be proposed:

$$O_O + H_{2(g)} = V_O^{k+} + ke^- + H_2O_{(g)}. \qquad (11)$$

The condition of lattice electroneutrality requires that:

$$n_e = \left[e^-\right] = k \cdot \left[V_O^{k+}\right], \qquad (12)$$

where $k = 1$ or 2 corresponds to singly or doubly ionized defects, respectively.

Applying the law of mass action to Equation 11 (with $k = 1$ or 2) gives power-law coefficients of $n = 1/2$ or 1/3 according to the relation:

Figure 8: a) Impedance spectra of 90 mol % SnO$_2$/10 mol % TiO$_2$ and 90 mol % TiO$_2$/10 mol % SnO$_2$ at 400 °C along with the electrical resistance as a function of the temperature (b, c) obtained on the basis of impedance measurements.

the Introduction section has to be taken into account. The second step given in a general form by Equation 2 is the surface reduction, which appears upon interaction with hydrogen and can be described in detail as follows [1,37]:

$$O_2^- + 2H_{2(g)} = 2H_2O_{(g)} + e^-, \qquad (5)$$

$$n_e = \frac{K_k}{p_{H_2O}} \left(p_{H_2} \right)^{\frac{1}{k+1}}. \tag{13}$$

Figure 9 and Table 4 demonstrate the results of the power-law analysis of the sensor response for: a) 90 mol % SnO_2/10 mol % TiO_2 and b) 10 mol % SnO_2/90 mol % TiO_2. In the log–log plot the dependence $R \propto p_{H_2}^{-n}$ can be fitted with a linear function. The values of the power coefficient n corresponding to

Table 4: Theoretical and experimental results of power law analysis.

| Theoretically predicted n	Equation	Form	Experimentally determined n	Figure	Interpretation
2	8	O_2^-	not observed	Figure 9	
1	9	O^-	0.88–1.26 for 90 mol % SnO_2/10 mol % TiO_2	Figure 9a	the ratio of O^-/O_2^- increases with temperature
1/2	10	O^{2-}	not observed for 90 mol % SnO_2/10 mol % TiO_2	Figure 9a	
1/2	13	$V_O^{\bullet}$	not observed for 10 mol % SnO_2/90 mol % TiO_2	Figure 9b	
1/3	13	$V_O^{\bullet\bullet}$	0.25–0.4 for 10 mol % SnO_2/90 mol % TiO_2	Figure 9b	our simplified model does not work here, the formation of point defects should be considered
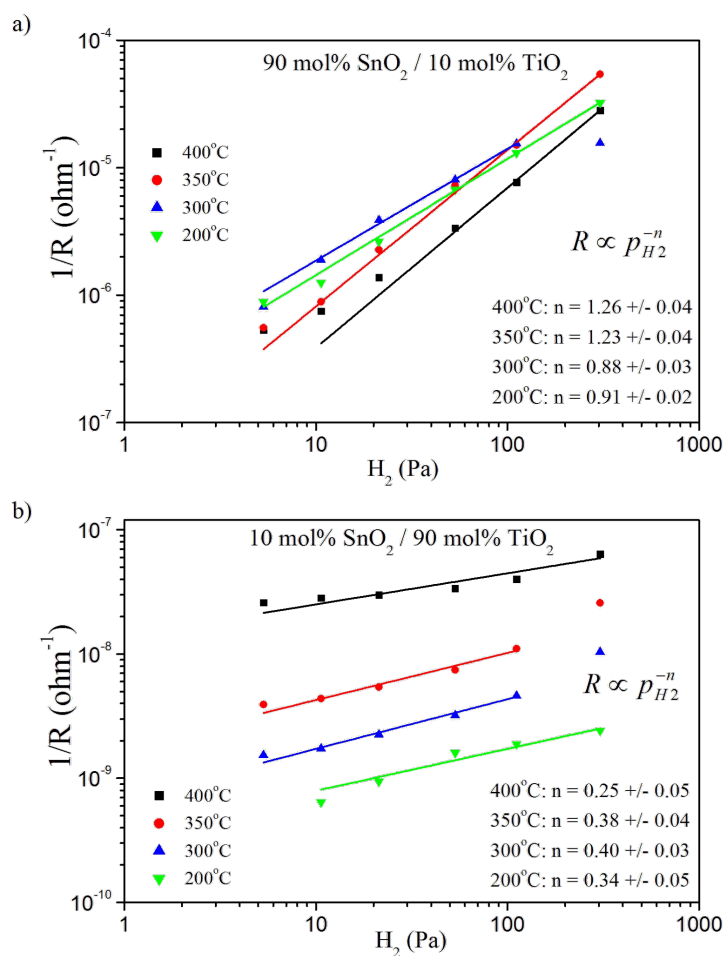
Figure 9: Log–log plot of the inverse of electrical resistance vs the hydrogen partial pressure for: a) 90 mol % SnO_2/10 mol % TiO_2 and b) 10 mol % SnO_2/90 mol % TiO_2 at temperatures of 200–400 °C.

the predominating form, along with the experimentally determined values (Table 4) can be attributed either to the specific oxygen form preadsorbed at the surface of the sensor or to the oxygen vacancies following the equations given above.

In our case the parameter n is around 1 for 90 mol % SnO_2/10 mol % TiO_2 at temperatures of 200–300 °C and slightly higher than 1 at 350 and 400 °C (Figure 9, Table 4). According to the literature [19] the adsorbed oxygen forms O_2^-, O^- and O^{2-} tend to predominate at the surface of SnO_2 with increasing temperature. Referring to this data one can conclude that in the case of 90 mol % SnO_2/10 mol % TiO_2, O_2^- and O^- are adsorbed and the ratio of O^-/O_2^- increases with temperature. Considering the 10 mol % SnO_2/90 mol % TiO_2 nanomaterial, n is in the range of 0.25–0.40. The reduction of titanium dioxide leads to the formation of oxygen vacancies.

For TiO_2-rich nanomaterials, the sensing properties cannot be explained within this simplified model. It appears that not only oxygen species preadsorbed on the surface of the semiconductor but also formation of point defects need to be considered.

Conclusion

1) TiO_2/SnO_2 heterostructures are well crystallized, anatase, rutile and cassiterite forms are present. Tin exhibits only the oxidation state 4+.

2) The detection threshold is below 1 ppm H_2 for SnO_2-rich heterostructures.

3) The addition of a small amount of SnO_2 to TiO_2 has a much more pronounced effect on the sensor response than the modification of SnO_2 by a small amount of TiO_2.

4) The recovery time of SnO_2-based heterostructures is longer than that of TiO_2-rich samples at higher H_2 concentrations.

5) TiO_2/SnO_2 heterostructures can be intentionally modified in order to meet the requirements for the successful detection of both small (SnO_2-rich) and large H_2 concentrations (TiO_2-rich).

6) The temperature T_{max} at which the semiconducting behavior begins to prevail upon water desorption/oxygen adsorption depends on the TiO_2/SnO_2 composition.

7) The electrical resistance of the sensor materials exhibits a power-law dependence on the partial pressure of H_2. In the case of 90 mol % SnO_2/10 mol % TiO_2, O_2^- and O^- ions are adsorbed and the ratio of O^-/O_2^- increases with temperature.

References

1. Radecka, M.; Zakrzewska, K.; Rękas, M. *Sens. Actuators, B* **1998,** *47,* 194–204. doi:10.1016/S0925-4005(98)00023-9
2. Shaposhnik, D.; Pavelko, R.; Llobet, E.; Gispert-Guirado, F.; Vilanova, X. *Sens. Actuators, B* **2012,** *174,* 527–534. doi:10.1016/j.snb.2012.05.028
3. Carotta, M. C.; Cervi, A.; Gherardi, S.; Guidi, V.; Malagu, C.; Martinelli, G.; Vendemiati, B.; Sacerdoti, M.; Ghiotti, G.; Morandi, S.; Lettieri, S.; Maddalena, P.; Setaro, A. *Sens. Actuators, B* **2009,** *139,* 329–339. doi:10.1016/j.snb.2009.03.025
4. Lyson-Sypien, B.; Czapla, A.; Lubecka, M.; Kusior, E.; Zakrzewska, K.; Radecka, M.; Kusior, A.; Balogh, A. G.; Lauterbach, S.; Kleebe, H.-J. *Sens. Actuators, B* **2013,** *187,* 445–454. doi:10.1016/j.snb.2013.01.047
5. Zeng, W.; Liu, T.; Wang, Z. *Physica E* **2010,** *43,* 633–638. doi:10.1016/j.physe.2010.10.010
6. Kusior, A.; Radecka, M.; Zych, Ł.; Zakrzewska, K.; Reszka, A.; Kowalski, B. J. *Sens. Actuators, B* **2013,** *189,* 251–259. doi:10.1016/j.snb.2013.07.029
7. Radecka, M.; Kusior, A.; Lacz, A.; Trenczek-Zajac, A.; Lyson-Sypien, B.; Zakrzewska, K. *J. Therm. Anal. Calorim.* **2012,** *48,* 1079–1084. doi:10.1007/s10973-011-1966-y
8. Carney, C. M.; Yoo, S.; Akbar, S. A. *Sens. Actuators, B* **2005,** *108,* 29–33. doi:10.1016/j.snb.2004.11.058
9. Kim, D. H.; Kim, W.-S.; Lee, S. B.; Hong, S.-H. *Sens. Actuators, B* **2010,** *147,* 653–659. doi:10.1016/j.snb.2010.03.065
10. Wen, Z.; Tian-mo, L. *Physica B* **2010,** *405,* 1345–1348. doi:10.1016/j.physb.2009.11.086
11. Wan, Y.; Liu, J.; Fu, X.; Zhang, X.; Meng, F.; Yu, X.; Jin, Z.; Kong, L.; Liu, J. *Talanta* **2012,** *99,* 394–403. doi:10.1016/j.talanta.2012.05.070
12. Wang, X.; Sang, Y.; Wang, D.; Ji, S.; Liu, H. *J. Alloys Compd.* **2015,** *639,* 571–576. doi:10.1016/j.jallcom.2015.03.193
13. Kusior, A.; Kollbek, K.; Kowalski, K.; Borysiewicz, M.; Wojciechowski, T.; Adamczyk, A.; Trenczek-Zajac, A.; Radecka, M.; Zakrzewska, K. *Appl. Surf. Sci.* **2016,** *380,* 193–202. doi:10.1016/j.apsusc.2016.01.204
14. Miller, D. R.; Akbar, S. A.; Morris, P. A. *Sens. Actuators, B* **2014,** *204,* 250–272. doi:10.1016/j.snb.2014.07.074
15. Jin, C.; Park, S.; Kim, H.; Ko, T.; Lee, C.; Jeong, B.-Y. *J. Korean Phys. Soc.* **2012,** *61,* 1370–1375. doi:10.3938/jkps.61.1370
16. Vaezi, M. R.; Shendy, S. K.; Ebadzadeh, T. *Indian J. Phys.* **2012,** *86,* 9–13. doi:10.1007/s12648-012-0002-9
17. Zhou, H.; Li, Z.; Niu, X.; Xia, X.; Wei, Q. *Ceram. Int.* **2016,** *42,* 1817–1826. doi:10.1016/j.ceramint.2015.09.145
18. Bielański, A.; Haber, J. *Catal. Rev.: Sci. Eng.* **1979,** *19,* 1–41. doi:10.1080/03602457908065099
19. Barsan, N.; Weimar, U. *J. Electroceram.* **2001,** *7,* 143–167. doi:10.1023/A:1014405811371

20. Yamazoe, N.; Shimanoe, K. *Sens. Actuators, B* **2008,** *128,* 566–573. doi:10.1016/j.snb.2007.07.036

21. Michalow, K. A.; Otal, E. H.; Burnat, D.; Fortunato, G.; Emerich, H.; Ferri, D.; Heel, A.; Graule, T. *Catal. Today* **2012,** *209,* 47–53. doi:10.1016/j.cattod.2012.10.007

22. Radecka, M.; Rekas, M.; Kusior, E.; Zakrzewska, K.; Heel, A.; Michalow, K. A.; Graule, T. *J. Nanosci. Nanotechnol.* **2010,** *10,* 1032–1042. doi:10.1166/jnn.2010.1865

23. Strobel, R.; Baiker, A.; Pratsinis, S. E. *Adv. Powder Technol.* **2006,** *17,* 457–480. doi:10.1163/156855206778440525

24. Akurati, K. K.; Vital, A.; Dellemann, J.-P.; Michalow, K.; Graule, T.; Ferri, D.; Baiker, A. *Appl. Catal., B* **2008,** *79,* 53–62. doi:10.1016/j.apcatb.2007.09.036

25. Michalow, K. A.; Vital, A.; Heel, A.; Graule, T.; Reifler, F. A.; Ritter, A.; Zakrzewska, K.; Rekas, M. *J. Adv. Oxid. Technol.* **2008,** *11,* 56–64. doi:10.1515/jaots-2008-0107

26. Lyson-Sypien, B.; Czapla, A.; Lubecka, M.; Gwizdz, P.; Schneider, K.; Zakrzewska, K.; Michalow, K.; Graule, T.; Reszka, A.; Rekas, M.; Lacz, A.; Radecka, M. *Sens. Actuators, B* **2012,** *175,* 163–172. doi:10.1016/j.snb.2012.02.051

27. Radecka, M.; Lyson, B.; Lubecka, M.; Czapla, A.; Zakrzewska, K. *Acta Phys. Pol., A* **2010,** *117,* 415–419. doi:10.12693/APhysPolA.117.415

28. Madelung, O., Ed. *Landolt–Börnstein Numerical Data and Functional Relationships in Science and Technology;* Springer: Berlin, Germany, 1983; Vol. 17, pp 133–149.

29. Herber, R. H. *Phys. Rev. B* **1983,** *27,* 4013–4017. doi:10.1103/PhysRevB.27.4013

30. Moreno, M. S.; Mercader, R. C. *Phys. Rev. B* **1994,** *50,* 9875–9881. doi:10.1103/PhysRevB.50.9875

31. Zakrzewska, K.; Radecka, M.; Przewoznik, J.; Kowalski, K.; Czuba, P. *Thin Solid Films* **2005,** *490,* 101–107. doi:10.1016/j.tsf.2005.04.035

32. Frederikse, H. P. R. *J. Appl. Phys.* **1961,** *32,* 2211–2215. doi:10.1063/1.1777045

33. Ishiguro, K.; Sasaki, T.; Arai, T.; Imai, I. *J. Phys. Soc. Jpn.* **1958,** *13,* 296–304. doi:10.1143/JPSJ.13.296

34. Brunauer, S.; Emmett, P. H.; Teller, E. *J. Am. Chem. Soc.* **1938,** *60,* 309–319. doi:10.1021/ja01269a023

35. Haber, J.; Stone, F. S. *Trans. Faraday Soc.* **1963,** *59,* 192–206. doi:10.1039/tf9635900192

36. Barsan, N.; Schweizer-Berberich, M.; Göpel, W. *J. Anal. Chem.* **1999,** *365,* 287–304. doi:10.1007/s002160051490

37. Kohl, D. *Sens. Actuators, B* **1989,** *18,* 71–113. doi:10.1016/0250-6874(89)87026-X